

In-Situ Imaging of Crack Growth with Piezoelectric Wafer Active Sensors

Victor Giurgiutiu*, Christopher Jenkins, James Kendall, Lingyu Yu
University of South Carolina, Columbia, SC 29208, victorg@sc.edu

Piezoelectric-wafer active sensors (PWAS) are small, inexpensive, non-invasive, elastic wave transmitters/receivers that can be easily affixed to a structure. PWAS are wide-band nonresonant devices that can selectively tune in various Lamb wave modes traveling in a thin-wall structure. PWAS can be wired into sensor arrays and connected to data concentrators and wireless communicators. They have the potential to bring about a revolution in structural health monitoring, damage detection, and non-destructive evaluation just as significant as ultrasonic inspection did 50 years ago. However, its development is not yet complete, and a number of issues have still to be resolved. This paper will present results obtained in using a PWAS phased array to in-situ image crack growth during a simulated structural health monitoring test. The fatigue crack growth experiment was set up on a 1000 mm by 1000 mm 2024-T3 1-mm thick aluminum plate. An initial pre-crack of 30 mm was grown under fatigue loading to a final length of 60 mm over a total of 58 kilocycles run at 10 Hz frequency in an MTS-810 testing machine. During the test, in-situ readings of the PWAS phased array were taken while the testing machine was running. The PWAS were excited with a 10-Vpp smoothed 3-count tone burst of 372 kHz, which excited the symmetric S0 Lamb-wave mode. To minimize the equipment requirement to just a single channel, the excitation of the PWAS array was performed in a round robin fashion. Simultaneously, all the PWAS were in term considered as receivers. In this way, an $N \times N$ matrix of signals was collected and stored. In the beginning, the received signals were unusable due to the high 10 Hz noise superposed by the testing process. Additional hardware was constructed to pre-filter the received signals prior to digitization. Consequently, usable signals with clear crack reflections were successfully collected. The received signals were post processed with the embedded ultrasonics structural radar (EUSR) algorithm to obtain a direct imaging of the crack in the test plate (similar to the C-scan from ultrasonic NDE, only that was obtained from a single location using a sweeping beam of focused Lamb waves. The imaging results were correlated with physical measurements of the crack size using penetrating liquid and a digital camera. Remarkable consistency was obtained. Subsequently, the results were used to predict further crack growth and make a prognosis of component failure using the structural health monitoring results.

I. INTRODUCTION

Structural health monitoring (SHM) is an emerging technology that is posed to transition the conventional ultrasonic nondestructive evaluation (NDE) methods to embedded systems that will be capable of performing on-demand interrogation of structural health. SHM requires the development of small, lightweight, inexpensive, unobtrusive, minimally invasive sensors to be embedded in the airframe with minimum weight penalty and at affordable costs. Such sensors should be able to scan the structure and identify the presence of defects and incipient damage. Current ultrasonic inspection of thin wall structures (e.g., aircraft shells, storage tanks, large pipes, etc.) is a time consuming operation that requires meticulous through-the-thickness C-scans over large areas. One method to increase the efficiency of thin-wall structures inspection is to utilize guided waves (e.g., Lamb waves) instead of the conventional pressure waves. Guided waves propagate along the mid-surface of thin-wall plates and shallow shells. They can travel relatively large distances with very little amplitude loss and offer the advantage of large-area coverage with a minimum of installed sensors. Guided Lamb waves have opened new opportunities for cost-effective detection of damage in aircraft structures, and a large number of papers have recently been published on this subject. Traditionally, guided waves have been generated by impinging the plate obliquely with a tone-burst

*Senior Member AIAA

from a relatively large ultrasonic transducer. However, conventional Lamb-wave probes (wedge and comb transducers) are relatively too heavy and expensive to consider for widespread deployment on an aircraft structure as part of a SHM system. Hence, a different type of sensors than the conventional ultrasonic transducers is required for the SHM systems. One way of addressing this need is through the piezoelectric wafer active sensors (PWAS), which are light weight and inexpensive transducers that can act as both transmitters and receivers of guided waves in thin wall structures.

This paper will show how PWAS can be used to detect crack growth in a thin-wall specimen through a direct imaging technique called *embedded ultrasonics structural radar* (EUSR). Ultrasonic guided waves (Lamb waves) transmitted and received with PWAS transducers will be used in conjunction with the phased-array principle to directly image a thin plate specimen being fatigued in a testing machine. The ultrasonic imaging will be done from a single location in which a PWAS phased array is installed. The imaging is done with the scanning beam of ultrasonic guided waves (Lamb waves) traveling in the plate. Thus, crack growth will be directly measured from the PWAS EUSR image. The ultrasonic phased-array image will be shown to compare with optical photos taken with a digital camera. Thus, a method for direct in-situ imaging of crack growth using permanently attached PWAS transducers will be presented.

The paper will start with a short review of the PWAS transducer principles. Emphasis will be placed on their interaction with the guided Lamb waves in the structure, and the PWAS capability to selectively tune into specific Lamb wave modes. Then, it will be shown how tuned Lamb wave modes (in particular, the low-dispersion S0 mode) can be used in conjunction with a PWAS phased array to directly image a thin-wall specimen with a steering beam generated in the PWAS array. In our particular application, an ingenious approach is taken to minimize the instrumentation requirements by using only one excitation channel, collecting the data in a round-robin fashion, and applying the phased array principles in virtual time during signal post-processing. The paper continues with a brief recall of the linear elastic fracture mechanics principles to be used in the design of the experimental specimen. The aim of this specimen design is to create the conditions under which sizable crack growth can be generated in a plate specimen during a reasonable testing period. Low-cycle fatigue principles, combined with fracture mechanics crack growth theory used in the specimen design are reviewed.

After these theoretical preliminaries, the paper will present the experimental setup used during the tests. The setup will consist of the testing machine used to apply the cyclic loading and the instrumentation used to collect the PWAS signals. Remarkably, the PWAS signal were collected during actual fatigue testing; thus, signal filtering and noise rejection methods had to be applied to extract the weak PWAS signal from the rather large noise created by the cycling testing and adjacent vibrations. The experimental procedure consisted of two steps: (a) validation of the crack growth assumptions, which will be done on a plain specimen without PWAS instrumentation; and (b) validation of the PWAS EUSR imaging of crack growth, which will be done on a fully instrumented second specimen. Discussion of the experimental results will indicate that the crack growth direct imaging using ultrasonic guided waves and an in-situ PWAS phased array will be shown to compare very well with the photos taken with a digital optical camera. Discussion of the results will also indicate the limitation of the present method, especially due to the size of the PWAS phased-array aperture, distance from the crack to the array, and crack orientation with respect to the array. A section on research summary, conclusions, and suggestions for further work will conclude the paper.

II. GUIDED-WAVE GENERATION/DETECTION WITH PIEZOELECTRIC WAFER ACTIVE SENSORS

In recent years, piezoelectric wafers permanently attached to the structure have been used for the guided waves generation and detection. We have named these devices *piezoelectric wafer active sensors* (PWAS), for lack of a better term [1]. PWAS are inexpensive, non-intrusive, un-obtrusive devices that can be used in both active and passive modes. In active mode, PWAS generated Lamb waves that can be used for damage detection through pulse-echo, pitch-catch, phased-array, or electromechanical (E/M) impedance techniques. In passive mode, PWAS can act as receivers of Lamb waves generated by low-velocity impacts or by acoustic emission at propagating crack tips.

PWAS operated on the piezoelectric principle that couples the electrical and mechanical variables in the material (mechanical strain, S_{ij} , mechanical stress, T_{kl} , electrical field, E_k , and electrical displacement D_j) in the form:

$$\begin{aligned} S_{ij} &= s_{ijkl}^E T_{kl} + d_{kij} E_k \\ D_j &= d_{jkl} T_{kl} + \epsilon_{jk}^T E_k \end{aligned} \quad (1)$$

where S_{ijkl}^E is the mechanical compliance of the material measured at zero electric field ($E = 0$), ε_{jk}^T is the dielectric permittivity measured at zero mechanical stress ($T = 0$), and d_{kij} represents the piezoelectric coupling effect. For embedded NDE applications, PWAS couple their in-plane motion, excited by the applied oscillatory voltage through the piezoelectric effect, with the Lamb-waves particle motion on the material surface. Lamb waves can be either quasi-axial (S_0 , S_1 , S_2 , ...), or quasi-flexural (A_0 , A_1 , A_2 , ...). Figure 1 shows the interaction between surface mounted PWAS and S_0 and A_0 guided Lamb waves.

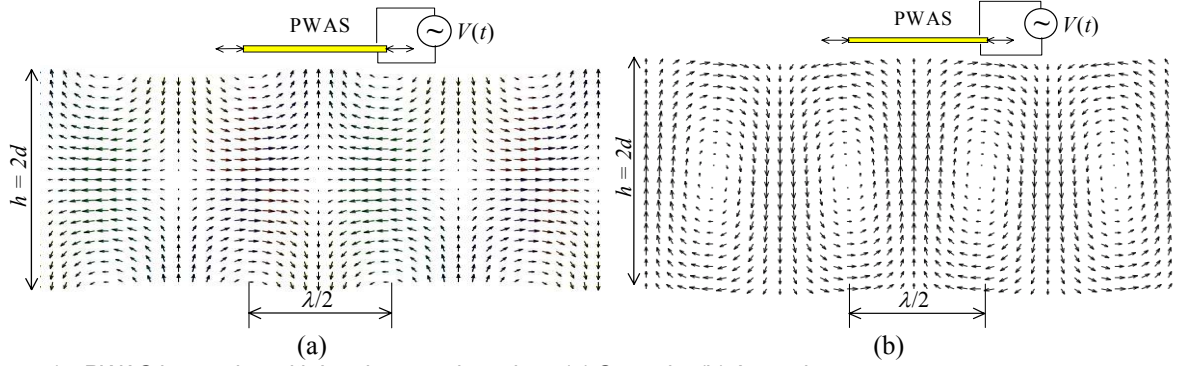


Figure 1 PWAS interaction with Lamb waves in a plate: (a) S_0 mode; (b) A_0 mode

The in-plane interaction between the PWAS and the guided Lamb waves is such that preferential tuning can be achieved when the representative PWAS dimensions are near an odd multiple of the half wavelength of certain Lamb-wave mode. Thus, multiple tuning can be achieved. Giurgiutiu [2] [3] developed the theory of the interaction of a rectangular PWAS with straight-crested Lamb waves and presented tuning prediction formulae based on trigonometric functions.

$$\varepsilon_x(x, t)|_{y=d} = -i \frac{a\tau_0}{\mu} \left[\sum_{\xi^S} \sin(\xi^S a) \frac{N_S(\xi^S)}{D_S'(\xi^S)} e^{i(\xi^S x - \omega t)} + \sum_{\xi^A} \sin(\xi^A a) \frac{N_A(\xi^A)}{D_A'(\xi^A)} e^{i(\xi^A x - \omega t)} \right] \quad (2)$$

where $N_S = \xi\beta(\xi^2 + \beta^2)\cos(\alpha d)\cos(\beta d)$; $N_A = \xi\beta(\xi^2 + \beta^2)\sin(\alpha d)\sin(\beta d)$

$$D_S = (\xi^2 - \beta^2)^2 \cos(\alpha d)\sin(\beta d) + 4\xi^2\alpha\beta\sin(\alpha d)\cos(\beta d)$$

$$D_A = (\xi^2 - \beta^2)^2 \sin(\alpha d)\cos(\beta d) + 4\xi^2\alpha\beta\cos(\alpha d)\sin(\beta d)$$

ξ^S and ξ^A are the zeros of D_S and D_A respectively. We can note that these are the solutions of the Rayleigh-Lamb equation. Raghavan and Cesnik [4] extended these results to the case of a circular transducer coupled with circular-crested Lamb waves and proposed corresponding tuning prediction formulae based on Bessel functions:

$$\varepsilon_r(r, t)|_{z=d} = \pi \frac{\tau_0 a}{\mu} e^{i\omega t} \left[\sum_{\xi^S} J_1(\xi^S a) \xi^S \frac{N_S(\xi^S)}{D_S'(\xi^S)} H_1^{(2)}(\xi^S r) + \sum_{\xi^A} J_1(\xi^A a) \xi^A \frac{N_A(\xi^A)}{D_A'(\xi^A)} H_1^{(2)}(\xi^A r) \right] \quad (3)$$

A comprehensive study of these prediction formulae in comparison experimental results has recently been performed by Bottai and Giurgiutiu [5]. Experiments were performed on large aluminum alloy plates using square, circular, and rectangular PWAS. Frequencies up to 700 kHz were explored. Two plate thickness were studied, 1.07 mm and 3.15 mm. In the thinner plate, only two Lamb wave modes, A_0 and S_0 were present in the explored frequency range. In the thicker plate, a third Lamb wave, A_1 , was also present. For example, Figure 2 shows the results for a 7-mm square PWAS placed on 1.07-mm 2024-T3 aluminum alloy plate. The experimental results (Figure 2a) show that a rejection of the highly dispersive A_0 Lamb wave mode is observed at around 200 kHz. At this frequency, only the S_0 mode is excited, which is very beneficial for pulse-echo studies due to the low dispersion of the S_0 mode at this relatively low value of the fd product. On the other hand, a strong excitation of the A_0 mode is observed at around 50 kHz. These experimental results were reproduced using Equation (2) with the assumption that the effective PWAS length is 6.4 mm (Figure 2b). The difference between the actual PWAS length and effective PWAS length is attributed to shear transfer/diffusion effects at the PWAS boundary.

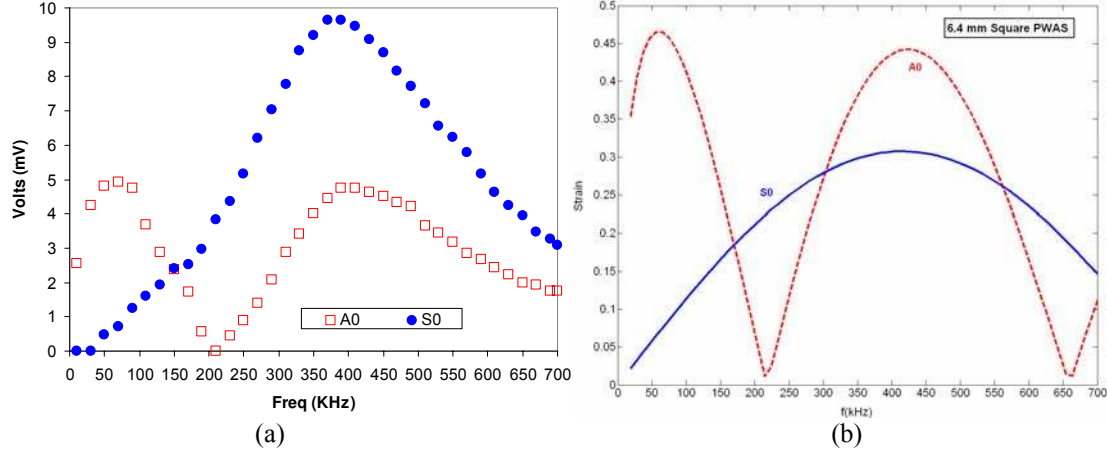


Figure 2: Lamb-wave tuning using a 7-mm square PWAS placed on 1.07-mm 2024-T3 aluminum alloy plate: (a) experimental results; (b) prediction with Equation (2) for 6.4 mm effective PWAS length.

III. EUSR STEERING BEAM DIRECT STRUCTURAL IMAGING WITH GUIDED WAVES PWAS PHASE-ARRAYS

By using Lamb waves in a thin-wall structure, one can detect the existences and positions of cracks, corruptions, delaminations, and other damage [6]. Because of the physical, mechanical, and piezoelectric properties of PWAS transducers, they act as both transmitters and receivers of Lamb waves traveling in the plate. Upon excitation with an electric signal, the PWAS generate Lamb waves into a thin-wall structure. The generated Lamb waves travel into the structure and are reflected or diffracted by the structural boundaries, discontinuities, and damage. The reflected or diffracted waves arrive back at the PWAS where are transformed into electric signals.

Table 1 $M \times M$ matrix of elemental signals generated in a round-robin in the PWAS phase-array

		Firing pattern (symbol T_i designates the transmitter that is activated)				
		T_0	T_1	T_2	...	T_{M-1}
Receivers	R_0	$p_{0,0}(t)$	$p_{0,1}(t)$	$p_{0,2}(t)$...	$p_{0,M}(t)$
	R_1	$p_{1,0}(t)$	$p_{1,1}(t)$	$p_{1,2}(t)$...	$p_{1,M}(t)$
	R_2	$p_{2,0}(t)$	$p_{2,1}(t)$	$p_{2,2}(t)$...	$p_{2,M}(t)$

	R_{M-1}	$p_{M-1,0}(t)$	$p_{M-1,1}(t)$	$p_{M-1,2}(t)$...	$p_{M-1,M-1}(t)$

Of particular interest is the phased-array implementation of this concept. The embedded ultrasonics structural radar (EUSR) is a phase-array application of the PWAS technology. The EUSR principles and initial results were reported extensively by Giurgiutiu and Bao [7] [8]. This idea is illustrated in Figure 4. An aluminum plate was instrumented with a number $M = 8$ PWAS transducers arranged in a linear phased array. The PWAS phased array is used to image the upper half of the plate and to detect structural damage using the PWAS EUSR phased array [8]. In order to implement the phased array principle, an $M \times M$ matrix of elemental signals $[p_{ij}(t)]$ is collected (Table 1). The elemental signals are obtained by performing excitation of one PWAS and detection on all the PWAS, in a round robin fashion. After the M^2 elemental signals are collected and stored in the computer memory, the phased array principle is applied in virtual time using the EUSR algorithm. In brief, this algorithm applies the “delay and sum” phased array principles on the matrix of M^2 elemental signals using the formula [8]:

$$s_R(t; \phi_0) = \sum_{i=0}^{M-1} \sum_{j=1}^{M-1} p_{ij}(t - \delta_i(\phi_0) - \delta_j(\phi_0)) = \sum_{i=0}^{M-1} \sum_{j=1}^{M-1} p_{ij}(t - i \cdot \Delta_0(\phi_0) - j \cdot \Delta_0(\phi_0)) \quad (4)$$

or

$$s_R(t; \phi_0) = \sum_{i=0}^{M-1} \sum_{j=1}^{M-1} p_{ij} (t - (i + j) \cdot \Delta_0(\phi_0)) \quad (5)$$

where ϕ_0 is the steering beam direction and

$$\Delta_0(\phi_0) = \frac{d}{c} \cos \phi_0 \quad (6)$$

is the time delay between two adjacent PWAS transducers. The other quantities in Equation (6) are the array pitch, d , and the wave speed, c .

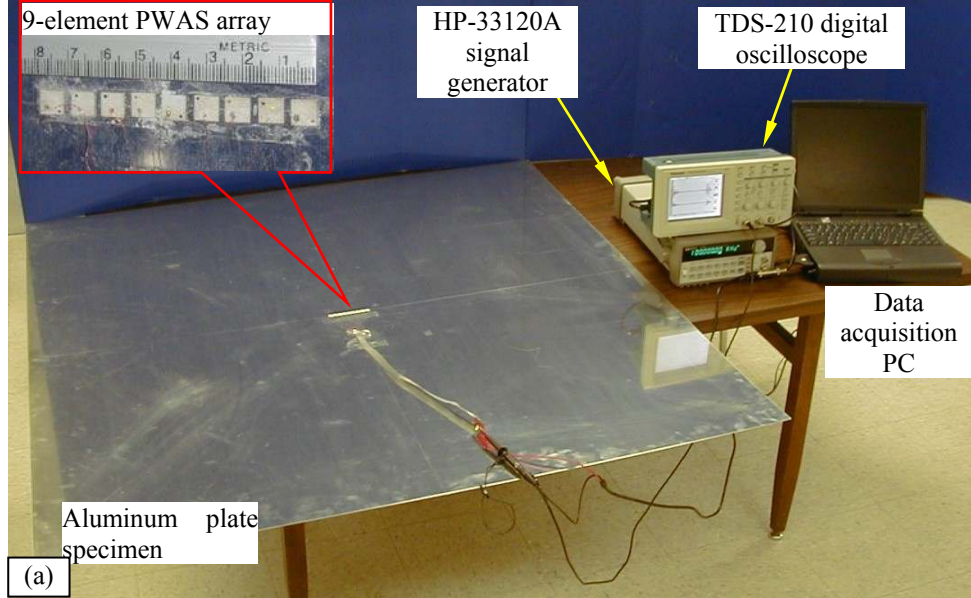


Figure 3 Specimen, PWAS-array, and instrumentation used for ; PWAS phased-array crack detection experiment [7]

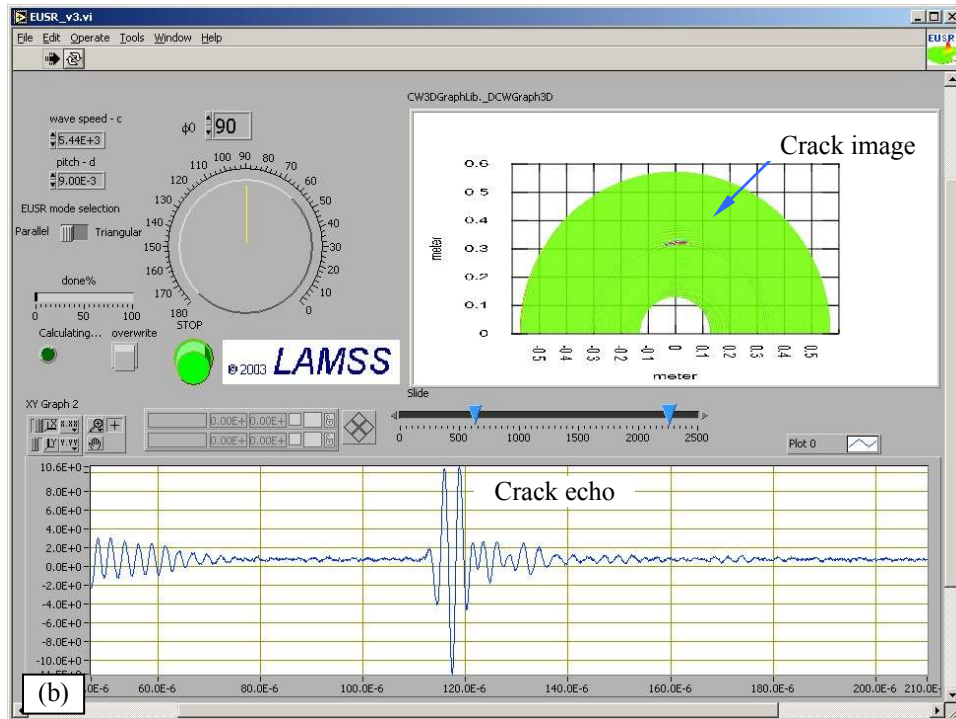


Figure 4 A-scan with crack echo and crack imaging as displayed by the EUSR GUI algorithm [7]

A LabVIEW program was constructed to implement the EUSR concept and the associated algorithm, as described in ref. [8]. The elemental signals of Table 1 are processed using the phased-array beam forming formulas as function of a variable azimuthal angle θ . The azimuthal angle θ is then allowed to vary in the range 0° to 180° . Thus, a sweep of the complete half plane is attained. At each azimuthal angle, an A-scan of the Lamb wave beam signal is obtained. If the beam encounters damage, reflection/diffraction from the damage will show as an echo in the A-scan. For example, the damage shown in Figure 3 is a 20-mm narrow slit simulating a through-the-thickness crack. The A-scan shown in Figure 4 indicates clearly the crack echo because the scanning beam is oriented at 90° . Azimuthal juxtaposition of all the A-scan signals creates an image of the half plane. The damage is clearly indicated as darker areas. Using the wave speed value $c = 5.440 \text{ mm}/\mu\text{s}$, the time domain signals are mapped into the space domain. A measuring grid is superposed on the reconstructed image to find the geometric position of the damage. Thus, the exact location of the damage can be directly determined.

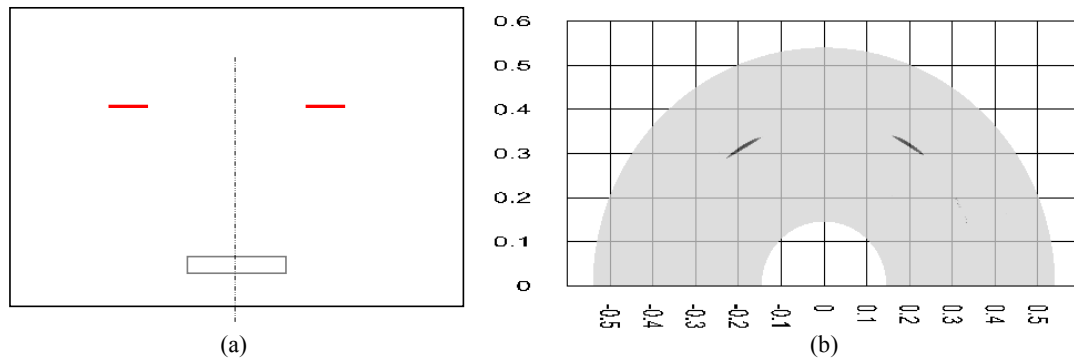


Figure 5 Detection of two cracks symmetrically placed offside of the PWAS phased array: (a) schematic; (b) EUSR image

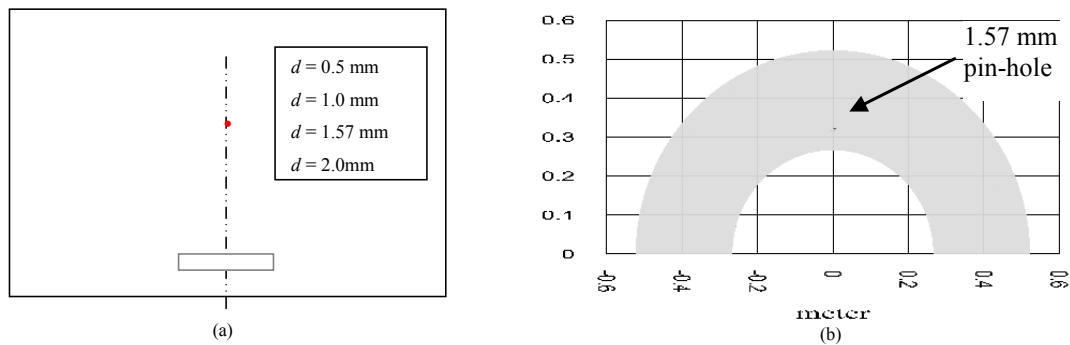


Figure 6 EUSR detection of pin-holes: (a) schematic of the experimental specimen; (b) EUSR GUI mapped image of the minimum detectable pin-hole with 1.57 mm diameter

The EUSR steering beam method based on PWAS phased-arrays has been refined to increase its power of detection for various structural defects [9]. Figure 5 shows the simultaneous detection of two cracks, which were placed symmetrically offside the PWAS phased array. Another concern was related to the probability of detection (POD) with this method. In an initial investigation, experiments were conducted to determine the smallest damage that the EUSR method could detect [9]. It was found that a pinhole as small as 1.57 mm can be detected directly and imaged relatively easily (Figure 6).

IV. REVIEW OF LINEAR ELASTIC FRACTURE MECHANICS PRINCIPLES

The stress intensity factor at a crack tip has the general expression

$$K(\sigma, a) = C\sigma\sqrt{\pi a} \quad (7)$$

where σ is the applied stress, a is the crack length, and C is a constant depending on the specimen geometry and loading distribution. It is remarkable that the stress intensity factor increases not only with the applied stress, σ , but also with the crack length, a . As the crack grows, the stress intensity factor also grows. If the crack growth too much, a critical state is achieved when the crack growth becomes rapid and uncontrollable. The value of K associated with rapid crack extension is called the *critical stress intensity factor*, K_c . For a given material, the onset of rapid crack extension occurs always at the same stress intensity value, K_c . For different specimens, having different initial crack lengths and geometries, the stress level, σ , at which rapid crack extension occurs, may be different. However, the K_c value will always be the same. Therefore, K_c is a property of the material. Thus, the condition for fracture to occur is that the local stress intensity factor, $K(\sigma, a)$ exceeds the value K_c , i.e.,

$$K(\sigma, a) \geq K_c \quad (8)$$

We see that K_c provides a single-parameter fracture criterion that allows the prediction of fracture. Although the detailed calculation of $K(\sigma, a)$ and determination of K_c may be difficult in some cases, the general concept of using K_c to predict brittle fracture remains nonetheless applicable. The K_c concept can be also extended to materials that possess some limited ductility, such as high-strength metals. In this case, the $K(\sigma, a)$ expression (7) is modified to account for a crack-tip plastic zone, r_Y , such that

$$K(\sigma, a) = C\sigma\sqrt{\pi(a + r_Y)} \quad (9)$$

where the maximum value of r_Y can be estimated as:

$$r_{Y\sigma} = \frac{1}{2\pi} \sqrt{\frac{K_c}{Y}} \quad (\text{plane stress}) \quad (10)$$

$$r_{Y\sigma} = \frac{1}{6\pi} \sqrt{\frac{K_c}{Y}} \quad (\text{plane strain}) \quad (11)$$

In studying the material behavior, one finds that the plane strain conditions give the lowest value of K_c , while the plane stress conditions can give K_c values that may be from two to ten times higher. This effect is connected with the degree of constraint imposed upon the material. The materials with higher constraint effects have a lower K_c value. The plain-strain condition is the condition with most constraint. The plain-strain K_c is also called the *fracture toughness* K_{Ic} of the material. Standard test methods exist for determining the material fracture toughness value. When used in design, fracture toughness criteria gives a larger margin of safety than elastic-plastic fracture mechanics methods such as (1) crack opening displacement (COD) methods; (b) R-curve methods; (c) J-integral method. However, the fracture toughness approach is more conservative: it is safer, but heavier. For a complete design analysis, the designer should consider, in most cases, both conditions: (a) the possibility of failure by brittle fracture; and (b) the possibility of failure by ductile yielding.

A Fracture Mechanics Approach to Crack Propagation

The concepts of linear fracture mechanics can be employed to analyze a given structure and predict the crack size that will propagate spontaneously to failure under the specified loading. This critical crack size can be determined from the critical stress intensity factor as defined in Equation (9). A fatigue crack that has been initiated by cyclic loading, or other damage mechanism, may be expected to grow under sustained cyclic loading until it reaches a critical size beyond which will propagate rapidly to catastrophic failure. Typically, the time taken by a given crack damage to grow to critical size represents a significant portion of the operational life of the structure. In assessing the useful life of a structure, several things are needed: (a) understanding of the crack initiation mechanism; (b) definition of the critical crack size, beyond which the crack propagates catastrophically (c) understanding the crack growth mechanism that makes a subcritical crack propagate and expand to the critical crack size. A plot of crack length versus number of cycles for various values of cyclic load is presented in Figure 7, where ΔP is the peak-to-peak range of the cyclic load. It is apparent from Figure 7 that a high cyclic-load value induces a much more rapid crack growth than a lower cyclic-load value. Also apparent in Figure 7 is that the crack growth has two distinct regions:

(i) A linear region, in which the crack growth is proportional with the number of cycles

(ii) A non-linear region, in which the crack growth is very fast and rapidly leads to failure

In analyzing fatigue crack growth, Paris and Erdogan [10] determined that the fatigue crack growth rate depends on the alternating stress and crack length:

$$\frac{da}{dN} = f(\Delta\sigma, a, C) \quad (12)$$

where $\Delta\sigma$ is the peak-to-peak range of the cyclic stress, a is the crack length, and C is a parameter that depends on mean load, material properties, and other secondary variables.

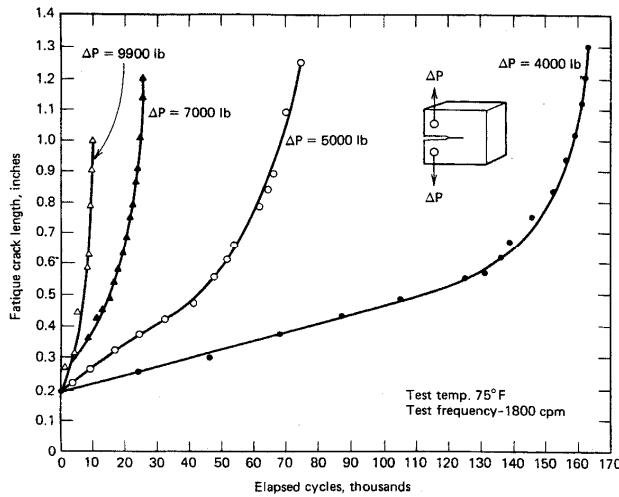


Figure 7: Effect of cyclic loading on crack growth in Ni-Mo-V alloy steel [11]

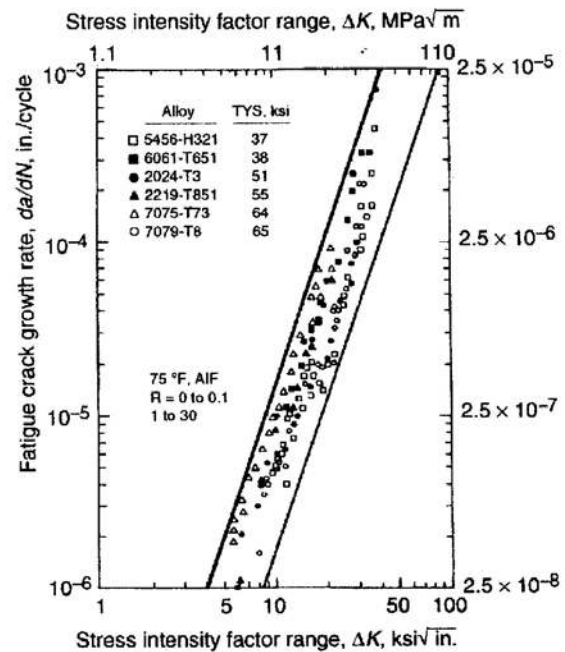
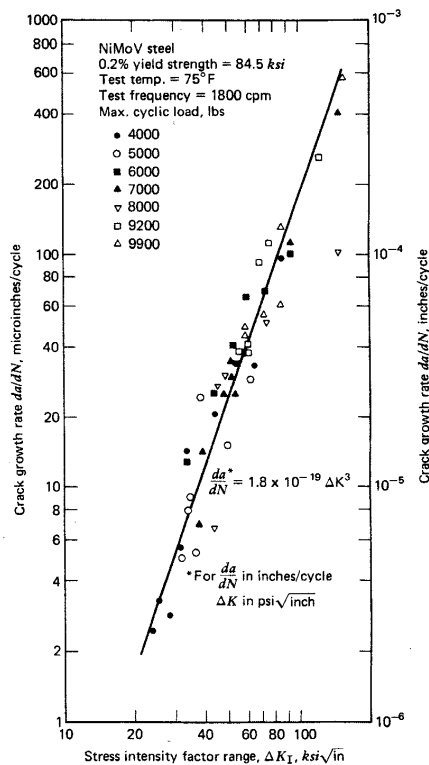


Figure 8: "Paris law" crack growth rate as function of cyclic stress-intensity factor peak-to-peak amplitude: (a) Ni-Mo-V alloy steel [11]; (b) aluminum alloys [12]

In view of Equation (7), it seems appropriate to assume that the crack-growth rate will depend on the cyclic stress intensity factor, K , i.e.,

$$\frac{da}{dN} = g(\Delta K) \quad (13)$$

where ΔK is the peak-to-peak range of the cyclic stress intensity factor. Figure 8 presents the plot of Equation (13) for the experimental data shown in Figure 7. It is remarkable that all the points, for various stress levels and various crack lengths, seem to follow a common law when plotted as crack-growth rate versus stress intensity factor. This remarkable behavior has become known as “Paris law”. Fatigue-crack growth-rate laws similar to that shown in Figure 8 have been reported for a wide variety of engineering materials. Since the curve in Figure 8 is linear on log-log scale, the corresponding Equation (13) can be written as:

$$\frac{da}{dN} = C_{EP}(\Delta K)^n \quad (14)$$

where n is the slope of the log-log line, and C_{EP} is an empirical parameter that depends upon material properties, test frequency, mean load, and some secondary variables. If the parameter C_{EP} and n are known, then one can predict how much a crack has grown after N cycles, i.e.,

$$a(N) = a_0 + \int_1^N C_{EP}(\Delta K)^n dN \quad (15)$$

where a_0 is the initial crack length.

In practice, it has been found that the crack growth follows three phases:

- (i) Crack nucleation
- (ii) Steady-state regime of linear crack growth
- (iii) Transition to the unstable regime of rapid crack extension and fracture.

Such a situation is depicted in Figure 9, where Region I corresponds to the crack nucleation phase, Region II to linear growth, and Region III to transition to the unstable regime. Threshold values for ΔK that delineate one region from the other seem to exist. As shown in Figure 9, the locations of these regions in terms of stress intensity factor values vary significantly from one material to another.

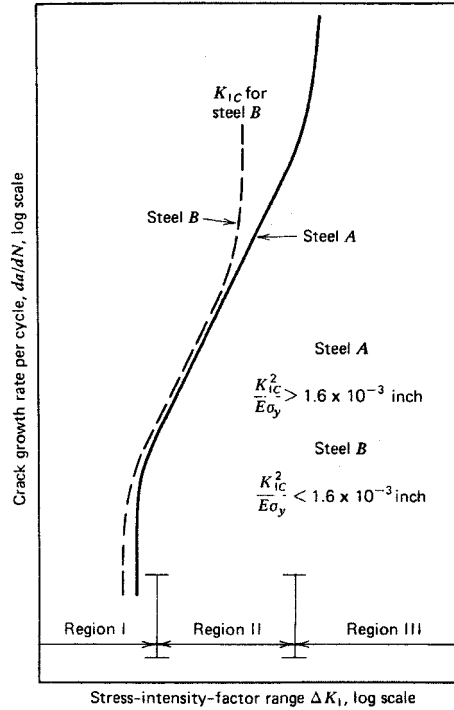


Figure 9: Schematic representation of fatigue crack growth in steel [13]

Paris law is widely used in engineering practice. Further studies have revealed several factors that also need to be considered when applying Paris law to engineering problems. Some of these factors are:

- Influence of cyclic stress ratio on the threshold value of ΔK
- Difference between constant-amplitude tests and spectrum loading
- Effect of maximum stress on spectrum loading
- Retardation and acceleration effects due to overloads

The influence of the stress ratio and threshold have been incorporated in the modified Paris law [14]

$$\frac{da}{dN} = \frac{C_{HS}(\Delta K - \Delta K_{TH})^m}{(1-R)K_c - \Delta K} \quad (16)$$

where R is the stress ratio $\sigma_{\max}/\sigma_{\min}$, K_c is the fracture toughness for unstable crack growth under monotonic loading, ΔK_{TH} is the threshold cyclic stress intensity factor for fatigue propagation, and C_{HS} is an empirical parameter.

The difference between constant-amplitude loading and spectrum loading has been shown to depend on the maximum stress value. If the maximum stress is held at the same values in both constant-amplitude and spectrum loading, then the crack growth rates seem to follow the same law. However, if the maximum stress is allowed to vary, the spectrum loading results seem to depend strongly on the sequence in which the loading cycles are applied, with the overall crack growth being significantly higher for spectrum loading than for constant-amplitude loading [15]. The retardation effects due to overloads have been reported by several investigators as evidence of the *interaction effect* whereby fatigue damage and crack extension dependence on preceding cyclic load history. An interaction of considerable interest is the *retardation* of crack growth as a result of the application of occasional cycles of crack-opening overload. Retardation is characterized by a period of reduced crack growth rate following the application of a peak load higher than the subsequent peak. The retardation has been explained by the inference that the overload will induce yield at the crack tip and will produce a zone of local plastic deformation in the crack tip vicinity. When the overload is removed, the surrounding material forces the yielded zone into a state of residual compression that tends to inhibit the crack growth under the subsequent loads P_2 of lower value. The crack growth rate will remain smaller until the growing crack has traversed the overload yield zone, when it returns to the normal value. Crack growth *acceleration*, on the other hand, may occur after crack-closing overloads. In this case, the overload yield zone will produce residual tension stresses which add to the subsequent loading and result in crack growth acceleration.

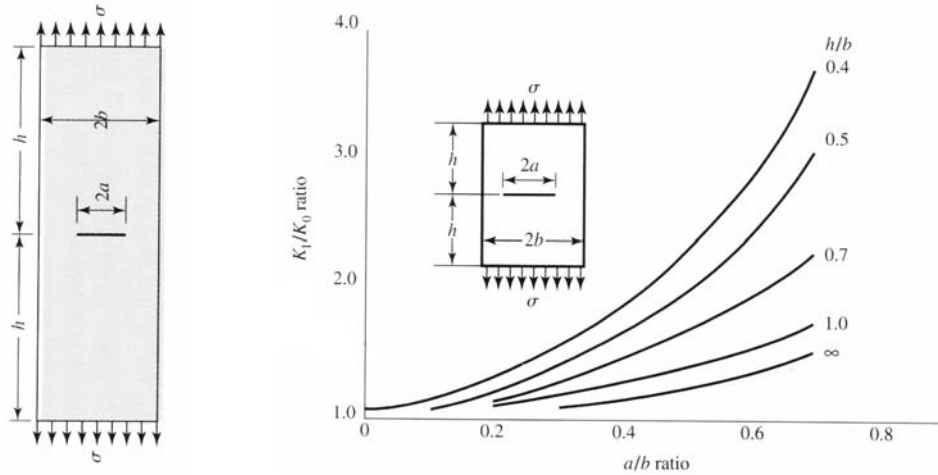


Figure 10 Plate (length = $2h$, width = $2b$), containing a central crack length of $2a$. Tensile stress σ acts in the longitudinal direction [16]

B Design of the experimental specimen

For the proposed experiment, we considered a rectangular specimen with a crack in the middle. For such a specimen, the equation for the stress-intensity for mode I testing is:

$$K_I = \beta \sigma \sqrt{\pi a} \quad (17)$$

Where σ is the applied tensile stress, a is half of the crack length, and $\beta = K_I / K_0$. The value of the parameter β has been determined numerically for a large variety of specimen geometries and can be found in the literature (Figure 10). In our case, we considered a 1-mm thick 2024-T3 aluminum specimen with dimensions 600 mm x 700 mm (24-in x 28-in). The specimen is loaded through a pre-existing loading jig that has seventeen 16-mm holes on two rows with 50-mm pitch and 38-mm row spacing (Figure 11). The presence of the loading holes imposes special requirements on the specimen design. (Since the loading jig already existed in the lab, the specimen design had to be adapted to the existing loading holes.) The loading holes weakened the specimen. Two strength concerns and one fracture concern had to be simultaneously considered with respect to the specimen loading holes:

- (a) The bearing strength of the hole
- (b) The shearing strength of the “plugs” between the holes and the sides of the specimen
- (c) The stress concentration at the holes should not promote fatigue cracking

In assessing these concerns, we used standard aircraft design practice guidelines for sheet metal joints [17].

The cyclic fatigue load was considered varying between an upper value, F_{\max} , and a lower value, F_{\min} . Since the specimen was of thin sheet-metal construction susceptible to buckling under compression, only tensile loads were considered. An R-ratio of 0.1 was selected ($R = F_{\min} / F_{\max}$). Thus, the alternate part of the cyclic loading was $F_a = 0.45F_{\max}$, whereas the mean part of the cyclic loading was $F_m = 0.55F_{\max}$. The strength concerns (a) and (b) were considered to be affected only by F_{\max} , whereas the stress concentration and crack propagation concern (c) was affected by both F_a and F_m . After performing the calculations, we concluded that a cyclic load of the specimen that would be safe for the bearing holes would be in the range $F_{\max} = 30,000$ kN, $R = 0.1$.

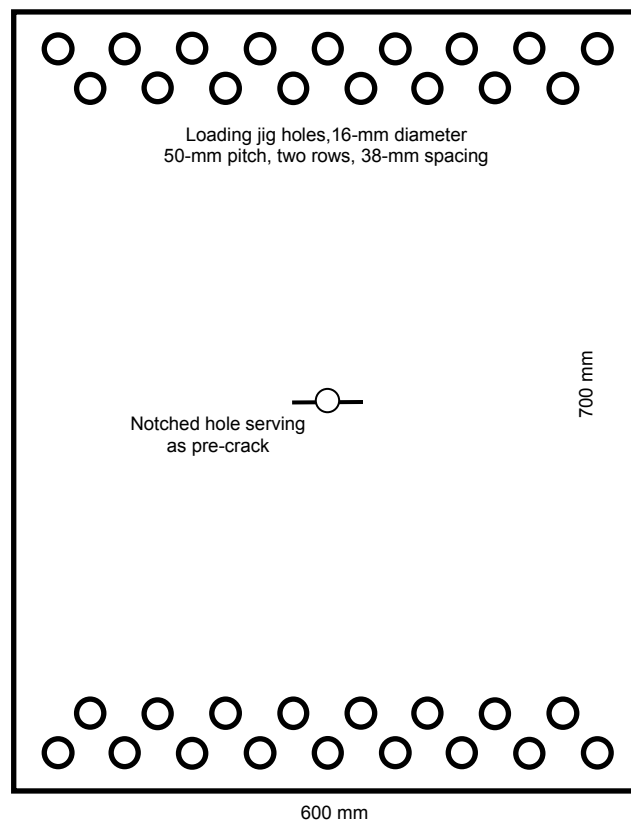


Figure 11 – Schematic of specimen VG-0 for assessing the crack growth rate parameters.

The length of the pre-crack made into the specimen center had to be calculated such that the applied cyclic load would promote crack propagation in the pre-crack. The cyclic load determined to be safe for the bearing holes was used to calculate the minimum pre-crack length that would promote crack propagation in the specimen. After performing the analysis, it was determined that an initial pre-crack length $2a = 50$ mm would be sufficient to achieve a crack intensity factor $\Delta K = 7.5 \text{ MPa}\sqrt{\text{m}}$ that will ensure an initial crack propagation at a comfortable rate according to Paris' Law of Figure 8a.

V. EXPERIMENTAL RESULTS

The experiments were conducted in two stages. In the first stage, experiments were aimed at determining the initial crack values and the loading conditions that will ensure crack nucleation and a controllable crack growth. In the second stage, the experiments were aimed at actually verifying that the crack growth can be directly imaged with the in-situ PWAS phased array using the EUSR algorithm. Of course, the first-stage experiments were aimed at giving a basis for the second-stage experiments, which were intended to utilize the crack growth parameters determined in the first stage.

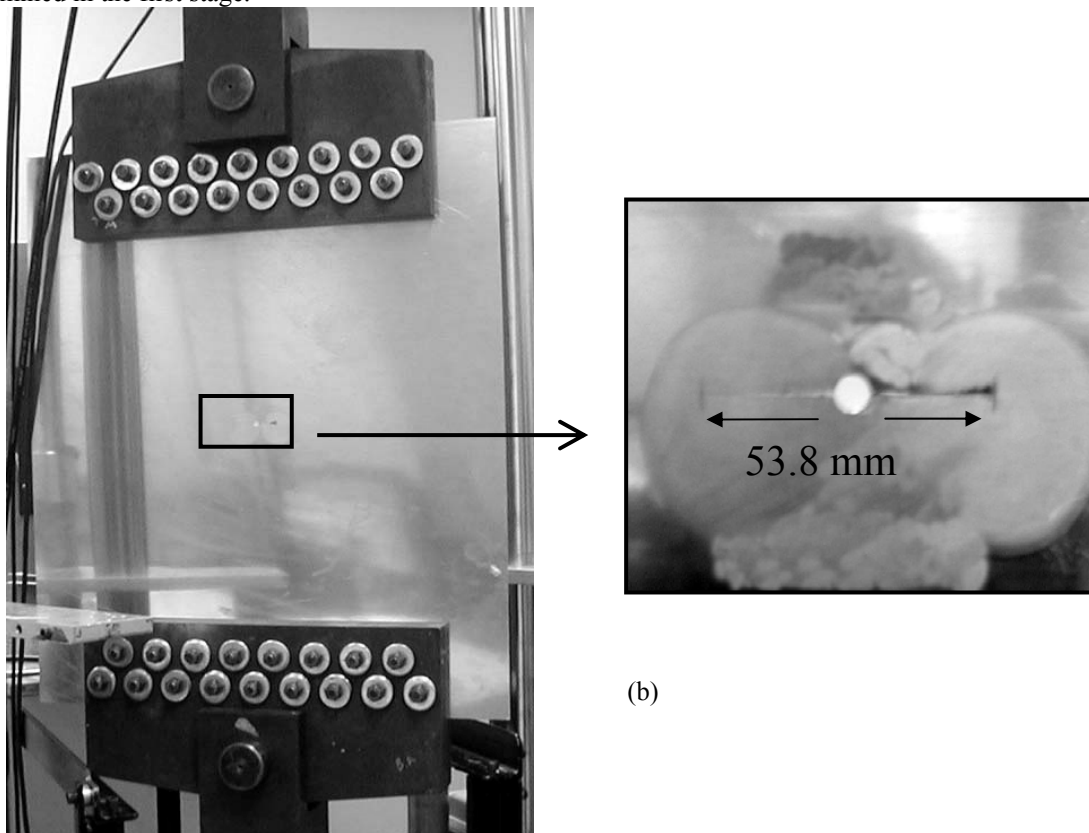


Figure 12 Experimental setup for fatigue testing without PWAS: (a) specimen VG-0 loaded in the MTS 810 testing machine; (b) notched hole serving as initial crack

A Stage I experiments: fatigue testing without PWAS

The stage I experiments were performed on specimen VG-0, without PWAS transducers (Figure 11). The specimen VG-0 was made of 2024-T3 aluminum sheet with a 1-mm thickness. The specimen size was 600 mm x 700 mm (24-in x 28-in). A notched hole was machined in the middle of the specimen. The diameter of the hole was 6.4 mm ($\frac{1}{4}$ -in) and the total pre-crack length was 53.8 mm (2.12-in). The specimen was placed in an MTS 810 testing machine, as shown in Figure 12a. Cycling loading was applied with $F_{\max} = 17,800$ N (4000 lbf) and $F_{\min} = 1,780$ N (400 lbf), i.e., $R = 0.1$. A total of 350 kcycles were applied at a frequency of 10 Hz. The crack length was measured periodically (every 20 kcycles) using a microscope attached to a digital caliper. The crack-growth results are shown in Figure 13 indicate that the crack growth behavior resembles Paris' Law. It is significant to note that the

crack growth started to accelerate after 300 kcycles, which is consistent with Paris' Law. At the end of the experiment, the crack has grown from the initial 54 mm to a final of approximately 210 mm. The corresponding stress intensity factors were $K_{initial} \cong 7.5 \text{ MPa}\sqrt{\text{m}}$ and $K_{final} \cong 15.3 \text{ MPa}\sqrt{\text{m}}$

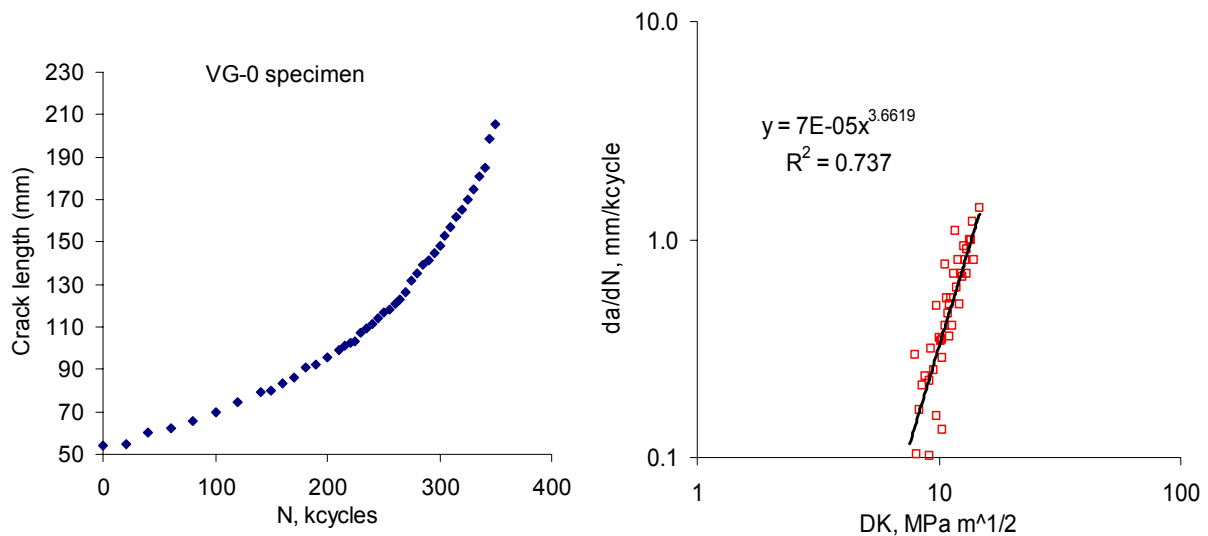


Figure 13 Crack growth results for specimen VG-0: (a) crack length vs. kcycles; (b) Paris Law fit

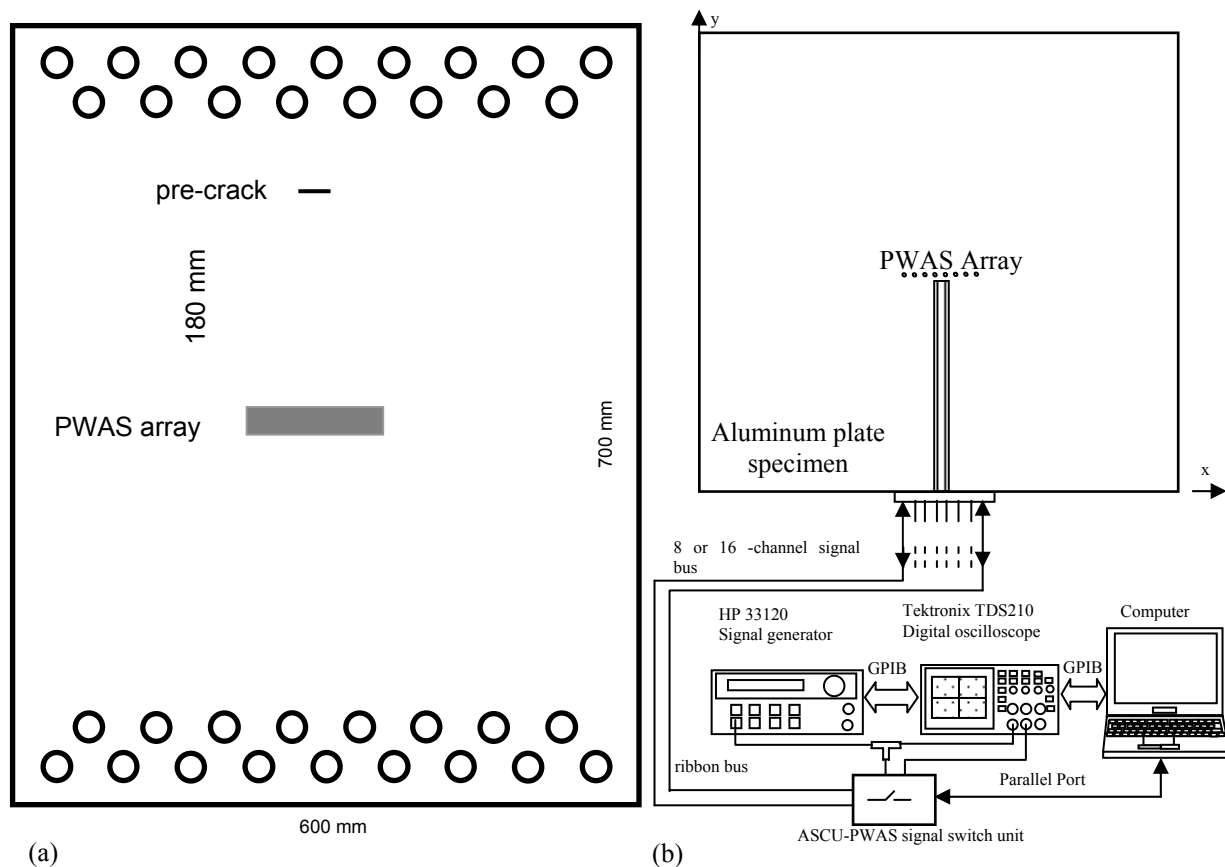


Figure 14 Schematic of experimental setup for fatigue testing with PWAS: (a) schematic of specimen VG-1 showing the installation of the PWAS array and the location of the precrack; (b) instrumentation schematics

B Stage II Experiments: Fatigue test with PWAS

The specimen for fatigue testing with PWAS transducers was named “VG-1” (Figure 14). The specimen construction is similar to that of specimen VG-0 used for fatigue testing without PWAS, i.e., 600 mm x 700 mm 1-mm thick 2024-T3 aluminum sheet with two rows of loading rows at each end. However, the specimen VG-1 presented the following differences from specimen VG-0:

- (a) The precrack was moved from the center to one side of the specimen, approximately 180 mm North of center
- (b) A 10-element PWAS array was placed in the center of the specimen

The pre-crack, made with a proprietary method, was 125 μm wide and 30 mm long. The 10-PWAS array was created by slicing two rectangular PZT wafers of dimensions 25 mm x 5 mm. The wafer thickness was 200 μm . The wafer had electrodes on both sides. The procedure consisted of first bonding the rectangular wafer to the plate at 340 mm (13.4”) from the plate edge, and then slicing the attached wafer with a scoring tool. After slicing, a phased array of ten PWAS, each approximately 5 mm (0.2-in) square, was obtained. The PWAS were numbered starting with PWAS 00 on the right and ending with PWAS 09 on the left. The instrumentation setup is shown in Figure 14b. It consisted of an HP 33120 signal generator, a TDS210 digital oscilloscope (serving as DAQ device) and a laptop computer.

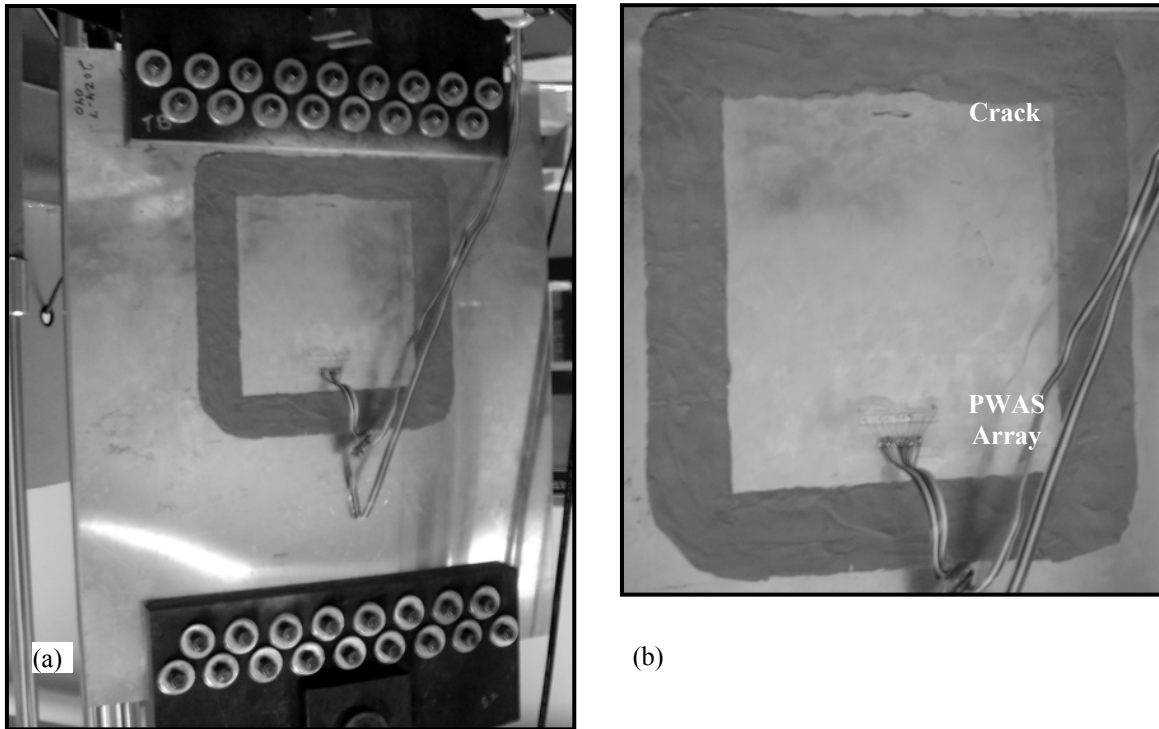


Figure 15 Experimental setup for fatigue testing with PWAS: (a) overall picture showing the specimen VG-1; (b) detail of the specimen showing the PWAS array, the crack, and the clay dam.

The instrumentation was used to implement the EUSR steering beam method for direct structural imaging with guided Lamb waves using the PWAS phased array (see Section III for details). In our case, the number of sensors used in the array was $M = 10$, i.e., from PWAS-00 through PWAS-09. Essential for the implementation of the EUSR algorithm is the round-robin collection of the M^2 array of elemental signals. The measurement procedure is performed in the following way (Figure 14b): a 3-count 372 kHz tone-burst excitation signal is synthesized in the function generator. (This frequency of the tone-burst signal corresponds to optimum tuning of the PWAS with the S0 Lamb-wave mode.) The tone-burst signal is sent to one PWAS in the array where is transformed into an S0 Lamb-wave packet. The Lamb-waves packet travels into the plate and is reflected at the plate boundary. The reflected Lamb-waves packet is received back at the PWAS array where is converted back into an electrical signal. The signals received at each PWAS in the array (including the transmitting PWAS) are collected by a DAQ device, e.g., a digital oscilloscope. To minimize instrumentation, the collection is done on only one DAQ channel using a round-robin procedure. This generates a column of M elemental signals in the M^2 elemental-signals array. After the

signal collection for one PWAS acting as exciter is finalized, the cycle is repeated for the other PWAS in a round-robin fashion. For, say, eight PWAS ($M=8$), there will be eight such measurement cycles necessary to complete the whole data collection process. It is apparent that the round-robin data collection can be tedious if done manually. However, considerable savings can be achieved if the process is automated. To automate the round-robin data collection, we used the automatic signal collection unit ASCU-PWAS equipment described in ref. [18].

To minimize the reflections from the loading holes and the plate boundary, a “clay frame” was placed around the PWAS and crack area (Figure 15).

1 Part I: Validation of the experimental method with PWAS

The first task in our experiment on fatigue with PWAS was to validate our experimental method. Two issues had to be proved:

- Determine if usable signals could be collected during the fatigue cycling
- Determine if PWAS would survive the fatigue cycling without disbonding from the specimen

The first issue was crucial to the experimental premises. The adverse factors to be clarified were connected with the relative weakness of the Lamb waves generated by our experimental setup in comparison with the rather large noise signals generated by the vibration of the specimen in the loading frame during the cyclic loading. Our initial tests proved that this was indeed so: the Lamb-wave signal was buried in the vibration noise. However, it was determined that the frequency of the noise (approximately, 10 to 100 Hz) is way outside the frequency band of the Lamb wave signals (300 to 400 kHz). Hence, we were able to use a high-pass filter to reject the noise while maintaining the useful Lamb-wave signal. The cutoff frequency of the high-pass filter was 1 kHz. A comparison of the signal before and after applying the filter is given in Figure 16. Figure 16 shows the graph of Pulse-Echo during fatigue cycling between PWAS 00 and PWAS 05 in the phased array with a filter taken while the specimen was under cyclic fatigue. Note that the reflection from the crack is clearly distinguishable. This has proven that data collection can be performed on line while the specimen is being tested in the fatigue machine, something that, so far, was not possible.

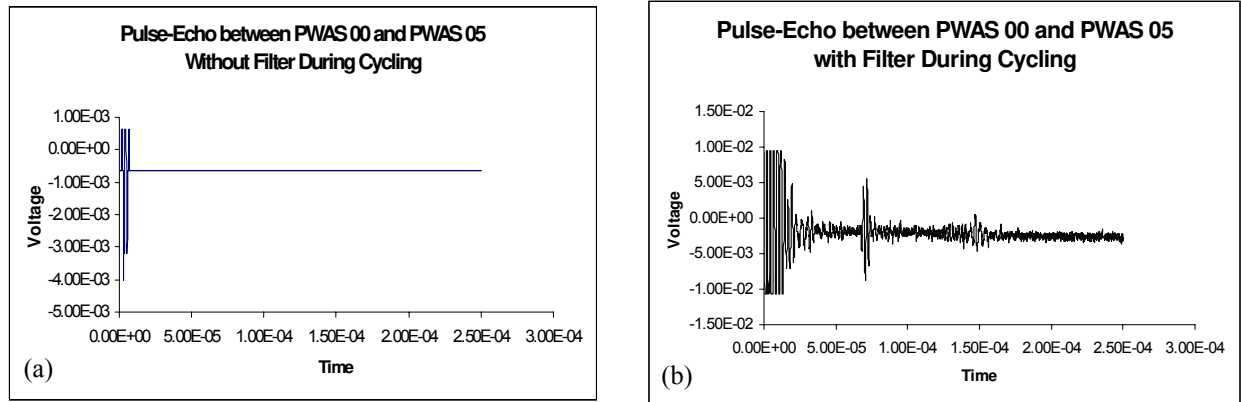


Figure 16 Effect of high-pass filtering on PWAS signal collection: (a) without filter, no Lamb-wave signals can be observed; (b) with filter, the Lamb-wave reflected from the crack can be easily identified

The second concern addressed during the fatigue testing with PWAS was that of PWAS survivability. In previous work [19], we proved that PWAS applied to dog bone fatigue specimens with stress concentrations can survive up to the specimen failure if proper bonding methods were used. Survival beyond 12 Mcycles was thus proved [19]. In present work, we used the same bonding methods used in ref. [19]: adhesive AE-10 from Measurements Group, Inc. and the corresponding surface preparation and curing procedure were used.

To verify the PWAS survival capabilities in the presence of fatigue loading, we selected the cyclic loading such that insignificant crack growth would occur. The selected loading was with $F_{\max} = 17,800$ N (4000 lbf) and $F_{\min} = 1,780$ N (400 lbf), i.e., $R = 0.1$. Since the precrack size was $2a = 25$ mm, the corresponding stress intensity factor range was $\Delta K \cong 5.8$ MPa $\sqrt{\text{m}}$. The PWAS readings were taken as follows. First, a baseline set of signals was taken. Then, the specimen was loaded into the tensile machine, and a second baseline was taken with the specimen under static load. Subsequently, the specimen was fatigued for 150 kcycles with readings of crack size being taken every 10 kcycles. The resulting crack-size readings are shown in the first part of Figure 17. It is notice from Figure 17 that during this part of the experiment no observable crack propagation was produced. By not propagating the crack, a comparison could be made between the baseline scans and the scans made during and after fatigue cycling. No

discernable difference could be observed in the EUSR imaging. Hence, it was concluded that the adhesion method was satisfactory, and that no PWAS disbonding occurred during tests.

2 Part 2: In-situ crack growth detection with PWAS phased-arrays during cyclic loading

The purpose of Part 2 of the fatigue testing with PWAS was to determine if PWAS phased array and the EUSR could detect and quantify the growth of the crack during fatigue loading. To achieve this, continued the testing of specimen VG-1, but increased the load applied to the specimen to with $F_{\max} = 35,600$ N (8000 lbf) and $F_{\min} = 3,560$ N (800 lbf), i.e., $R = 0.1$, again. Crack-size readings were taken at approximately every 2 kcycles. Under these conditions, the crack grew rapidly from 25 mm to 143 mm over a 85-kcycles duration (Figure 17). The total duration of the fatigue testing was 235 kcycles, of which: 150 kcycles at low load values and no crack growth; 85 kcycles at high load value and crack growth.

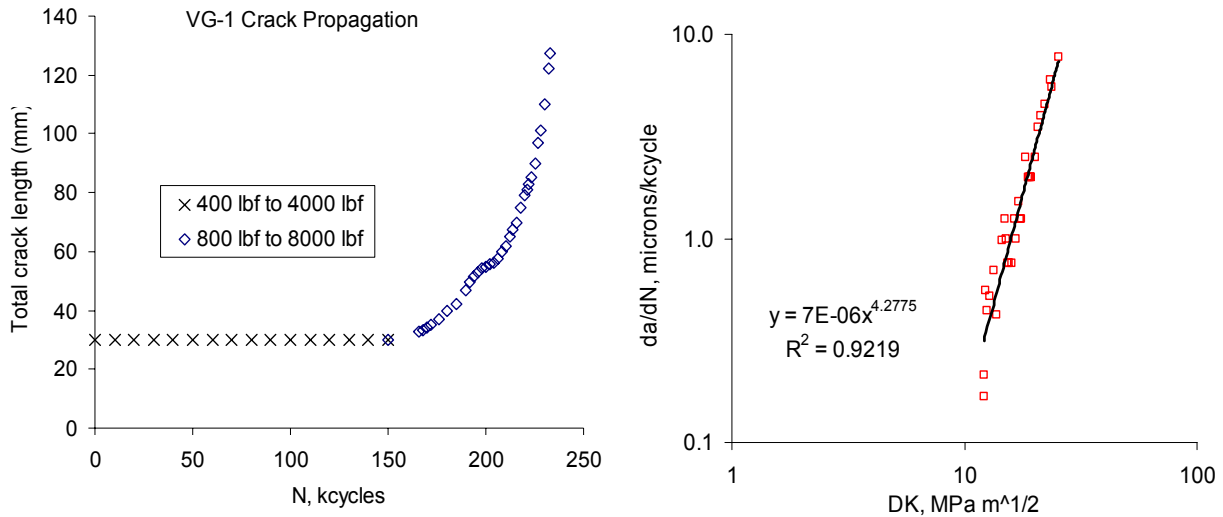


Figure 17 Crack growth history for the specimen VG-1 instrumented with a PWAS phased-array: (a) crack length vs. kcycles; (b) Paris Law fit

Recordings of the PWAS phased-array ultrasonic signals were taken at selected intervals during this crack growth process. Every reading was taken with two loading conditions: (a) under dynamic conditions, i.e., with the testing machine operating under cyclic loading; and (b) under static conditions, i.e., with the testing machine held at the mean load. As the crack growth became more rapid, the interval between two consecutive recordings also shortened. Imaging of the crack growth as resulting from the ultrasonic Lamb-wave phased-array interrogation was reconstructed with the EUSR algorithm. A digital camera optical photograph of the actual crack was also taken, in parallel with the EUSR imaging.

The crack-growth results shown in Figure 17 indicate that the crack growth behavior resembles Paris' Law. It is significant to note that the crack growth started to accelerate after 220 kcycles, which is consistent with Paris' Law. At the end of the experiment, the crack has grown from the initial length of 25 mm to a final length of 143 mm. The corresponding stress intensity factors were $\Delta K_{\text{initial}} \cong 11.6 \text{ MPa}\sqrt{\text{m}}$ and $\Delta K_{\text{final}} \cong 25.3 \text{ MPa}\sqrt{\text{m}}$.

The EUSR algorithm and the associated software program were used to process the PWAS phased array data and image the crack at each cycle value scanned. Figure 19 shows a progression of cracks sizes, as they developed in the specimen VG-1 during the fatigue testing. The upper row of images contains the optical photos taken with a digital camera. The lower row of images contains the EUSR images of the crack obtained with the PWAS phased-array method. It is apparent that the two rows of images are in very good correlation.

The EUSR graphical user interface (GUI) was used to obtain an estimation of the crack size. Figure 18 is a screen capture of the EUSR GUI. The threshold value and the values δ and θ of the "dial angles" are controlled from this GUI. First, an approximate position of the crack edge is obtained with the azimuth dial. If the azimuth dial is turned to an angle where the synthetic beam find a target and gets a reflection, then the A-scan image will show a reflection echo as illustrated in Figure 18a. After a threshold value was chosen, the θ and δ angles were adjusted such that their rays touched the left and right tips (respectively) of the crack image reproduced in the EUSR GUI.

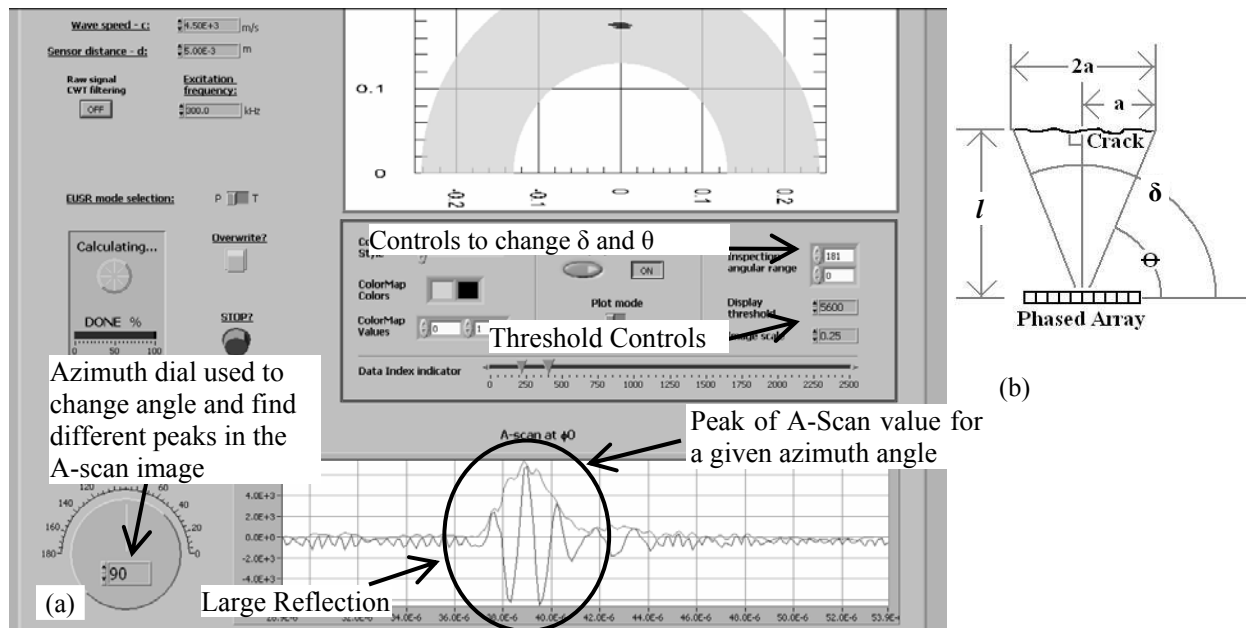


Figure 18 Determination of crack size from the GUI of the PWAS EUSR program: (a) annotated screen capture showing the angles and threshold controls of EUSR GUI; (b) schematic indicating the θ and δ angles in relation to the crack length, $2a$ and distance to the target, l .

The length of the crack thus estimated using the EUSR GUI can be easily found using the geometry shown in Figure 18b, i.e.,

$$2a_{EUSR} = l(\tan \delta + \tan \theta) \quad (18)$$

In our experiment, the distance between the array and the crack was $l = 180$ mm. Hence, the EUSR estimated crack length could be calculated at various numbers of cycles.

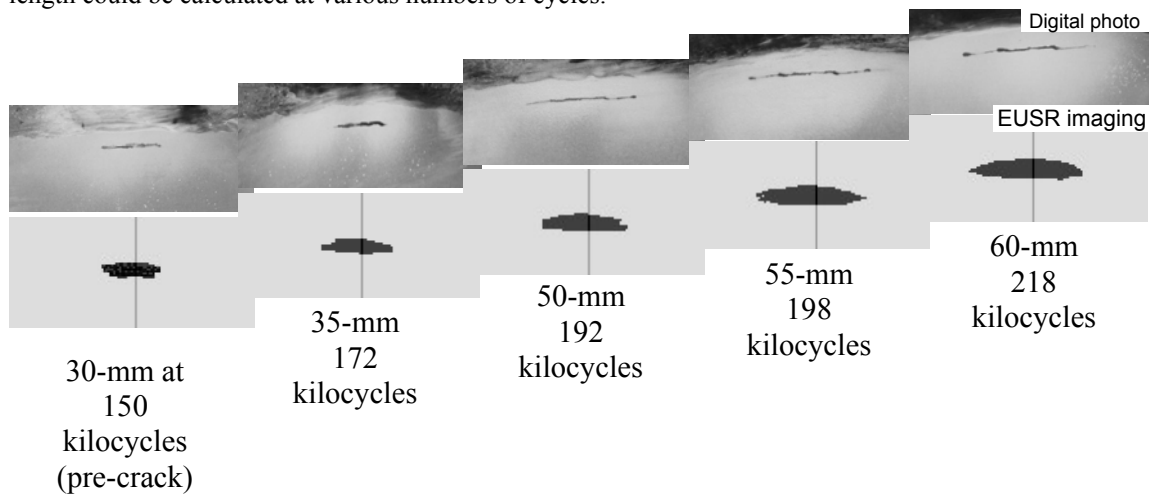


Figure 19 Comparison between images taken optically and scanned images using EUSR

During data processing, it was noticed that, from 150,000 cycles to 200,000 cycles to, the threshold remained the same and the EUSR image of the crack, which grew with the number of cycles, and was close to the actual crack size, as measured with optical means. However, after the crack grew to about 55 mm, the EUSR image did not grow with the same threshold and the threshold had to be changed to image the crack with dimensions that were comparable to the optical measurements. Several samples of the EUSR images with corresponding optical crack images are given in Figure 19. The EUSR crack-length image for up to ~ 200 kcycles is close to being accurate, the EUSR crack length image did not significantly change from the EUSR image at 200,000 cycles. This could be due

to phased-array aperture effects (Figure 20). The reflections of the wave from the crack are stronger when the crack is directly in front of the PWAS array. When the crack grows beyond the length of the PWAS array, the reflections are weaker and the image of the crack length cannot be seen at a high threshold because the high threshold will cover the weaker reflections (see Figure 20). If the threshold is not changed when the crack length is larger than the PWAS array, the EUSR crack image will remain at the same length as the PWAS array for any crack length longer than the PWAS array. An intuitive explanation of this phenomenon is as follows: Think of the PWAS array as someone looking at an object directly in front of the eyes. The person can clearly see the object directly in front of them, but cannot clearly see objects to the side or that are not directly in front. Although the objects are not clearly seen, the person is still aware of the objects. The same seems to be true with the PWAS array, it can see images that are not directly in front of it at an appropriate threshold but not well enough to quantify the accurate length.

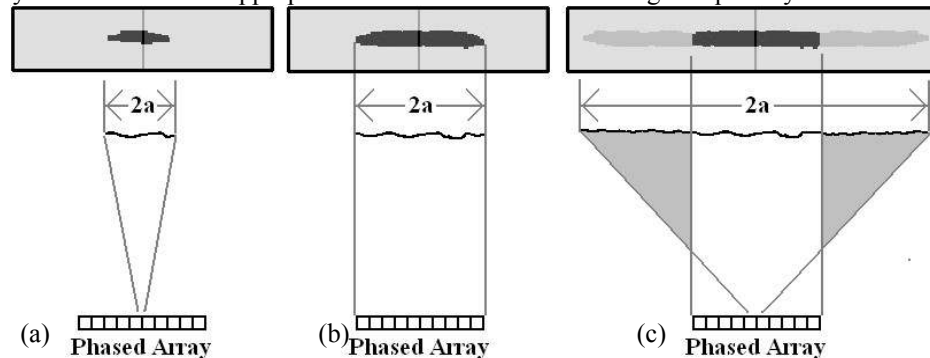


Figure 20 Aperture effects on PWAS phased-array EUSR imaging of crack length (a) if crack is less than array aperture the crack is well imaged; (b) borderline case when crack and aperture are equal in length; (c) if crack length exceeds array aperture, the EUSR image of the crack does not grow proportionally with the crack length if the threshold is kept constant. Threshold had to be lowered to see the grayed out image of the crack.

VI. IMPROVED DIAGNOSIS AND PROGNOSIS THROUGH STRUCTURAL HEALTH MONITORING

A Damage Tolerance, Fracture Control and Life-cycle Prognosis

A *damage tolerant* structure has a design configuration that minimizes the loss of aircraft due to the propagation of undetected flaws, cracks, and other damage. To produce a damage-tolerant structure, two design objectives must be met:

- (a) Controlled safe flaw growth, or safe life with cracks
- (b) Positive damage containment, i.e., a safe remaining (residual) strength

These two objectives must be simultaneously met in a judicious combination that ensures effective fracture control. Damage-tolerant design and fracture control includes:

- (i) Use of fracture-resistant materials and manufacturing processes
- (ii) Design for inspectability
- (iii) Use of damage-tolerant structural configurations such as multiple load paths or crack stoppers (Figure 21)

In the application of fracture control principles, the basic assumption is that flaws do exist even in new structures and that they may go undetected. Hence, any member in the structure must have a *safe life* even when cracks are present. In addition, flight critical components must be *fail-safe*. The concept of **safe life** implies the evaluation of the expected lifetime through margin-of-safety design and full-scale fatigue tests. The margin of safety is used to account for uncertainties and scatter. The concept of **fail-safe** assumes that flight critical components cannot be allowed to fail, hence alternative load paths are supplied through redundant components. These alternative load paths are assumed to be able to carry the load until the failure of the primary component is detected and a repair is made.

B Fracture Control through NDI/NDE

In-service inspection procedures play a major role in the fail-safe concept. Structural regions and elements are classified with respect to required nondestructive inspection (NDI) and nondestructive evaluation (NDE) sensitivity. Inspection intervals are established on the basis of crack growth information assuming a specified initial flaw size and a “detectable” crack size, a_{det} , the latter depending on the level of available NDI/NDE procedure and equipment.

Cracks larger than a_{det} are presumed to be discovered and repaired. The inspection intervals must be such that an undetected flaw will not grow to critical size before the next inspection. The assumptions used in the establishment of inspection intervals are:

- All critical points are checked at every inspection
- Cracks larger than a_{det} are all found during the inspection
- Inspections are performed on schedule
- Inspection techniques are truly non-damaging

In practice, these assumptions are sometimes violated during in-field operations, or are impossible to fulfill. For example, many inspections that require extensive disassembly for access may result in flaw nucleation induced by the disassembly/reassembly process. Some large aircraft can have as many as 22,000 critical fastener holes in the lower wing alone [21]. Complete inspection of such a large number of sites is not only tedious and time consuming, but also subject to error born of the boredom of inspecting 20,000 holes with no serious problems, only to miss one hole with a serious crack (sometimes called the “rogue” crack). Nonetheless, the use of NDI/NDE techniques and the establishment of appropriate inspection intervals have progressed considerably. Recent developments include automated scanning systems and pattern recognition method that relieve the operator of the attention-consuming tedious decision making in routine situations and allow the human attention to be concentrated on truly difficult cases. Nevertheless, the current practice of scheduled NDI/NDE inspections leaves much to be desired.

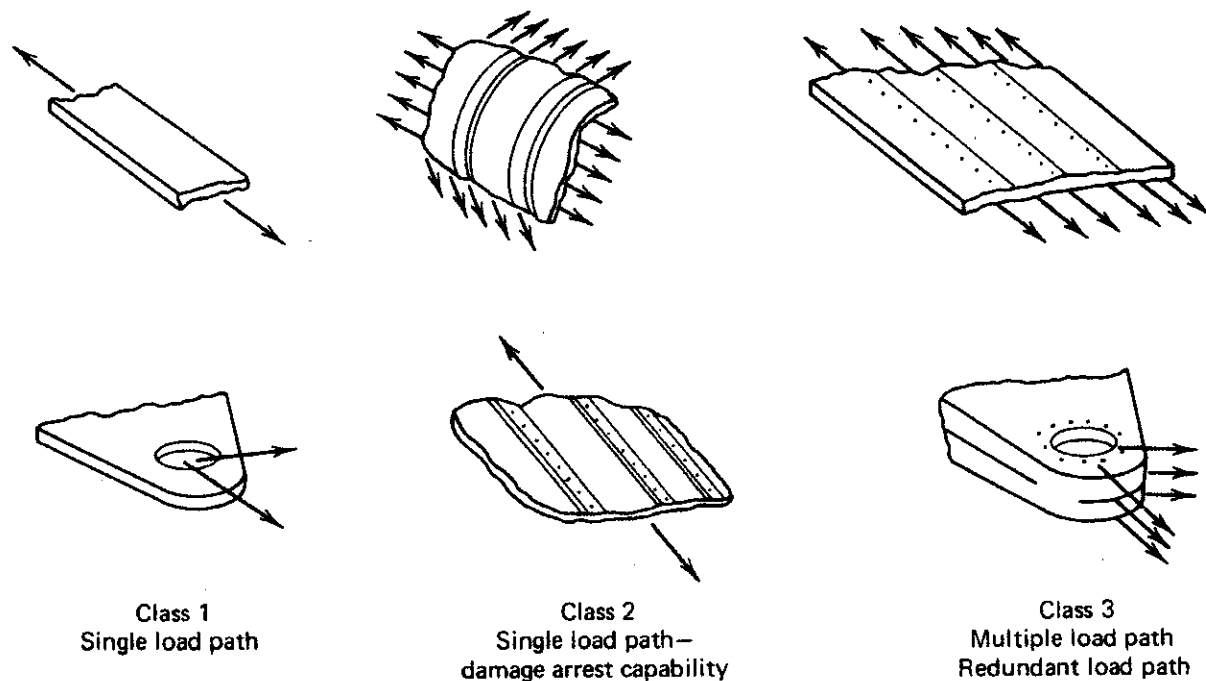


Figure 21: Structural types based on load path [20]

C Life-cycle Prognosis Based on Fatigue Tests

The estimated design life of an aircraft is based on full scale fatigue testing of complete test articles under simulated fatigue loading. The benefits of full-scale fatigue testing include:

- Discover fatigue critical elements and design deficiencies
- Determine time intervals to detectable cracking
- Collect data on crack propagation
- Determine remaining safe life with cracks
- Determine residual strength
- Establish proper inspection intervals
- Develop repair methods

The structural life proved through simulation test should be longer by a factor from two to four than the design life. Full-scale fatigue testing should be continued over the long term such that fatigue failures in the test article will stay ahead of the fleet experience by enough time to permit the redesign and installation of whatever modifications are required to prevent catastrophic fleet failures. However, full-scale fatigue testing of an article such as a newly designed aircraft is extremely expensive. In addition, the current aircraft in our fleets have exceeded the design fatigue life, and hence are no longer covered by the full-scale fatigue testing done several decades ago.

D Perceived SHM Contributions the Structural Diagnosis and Prognosis

Structural health monitoring (SHM) could have a major contribution to the structural diagnosis and prognosis. Although NDE methods and practices have advanced remarkably in recent years, some of their inherent limitations still persist. NDI/NDE inspection sensitivity and reliability are driven by some very practical issues when dealing with actual airframes. Field inspection conditions may be quite different when compared to laboratory test standards.

Perhaps the major limitation of current NDI/NDE practices is the fact that NDI/NDE, as we know it, cannot provide a continuous assessment of the structural material state. This limitation is rooted in the way NDI/NDE inspections are performed: the aircraft has to be taken off line, stripped down to a certain extent, and scanned with NDI/NDE transducers. This process is time-consuming and expensive. This situation could be significantly improved through the implementation of a SHM system. Having the SHM transducers permanently attached to the structure (even inside closed compartments), would allow for structural interrogation (scanning) to be performed on demand, as often as needed. In addition, a consistent historical record can be accumulated since these on-demand interrogations are done always with the same transducers which are placed in exactly the same locations and interrogated in the same way.

SHM could provide an advanced utilization of the existing sensing technologies to add progressive state change information to a system reasoning process from which we can infer component capability and predict its future safe-use capacity [22]. Through monitoring the state of structural health, we can achieve a historical database and acquire change information to assist in the system reasoning process. Advanced signal processing methods can be used to detect characteristic changes in the material state and make that state-change information available to the prognosis reasoning system. The concept of change detection can be used to characterize the material state by identifying critical features that show changes with respect to a reference state that is stored in the information database and updated periodically. When this is performed in coordination with existing NDI/NDE practices, the structural health monitoring information performed in between current inspection intervals will provide supplementary data that would have a densifying effect on the historical information database.

Another advantage of implementing SHM systems is related to the nonlinear aspects of structural crack propagation. Most of the current life prognosis techniques are based on linear assumptions rooted in laboratory tests performed under well defined conditions. However, actual operational conditions are far from ideal, and incorporate a number of unknown factors such as **constraint effects, load spectrum variation, and overloads**. These effects are in the realm of nonlinear fracture mechanics and make the prediction very difficult. However, the dense data that can be collected by an SHM system could be used as feedback information on, say, the crack growth rate (as illustrated in this paper), and could allow the adjustment of the basic assumptions to improve the crack-growth prediction laws.

VII. SUMMARY AND CONCLUSIONS

Structural health monitoring (SHM) is an emerging technology with great potential in structural material diagnosis and prognosis. SHM systems can be passive or active. Active SHM systems rely on structural interrogation using active sensors (transducers) that can transmit and receive ultrasonic Lamb waves traveling at large distances in the structural material. Active SHM emulates the ultrasonic NDI/NDE practices for detecting structural damage, but have the advantage of being able to do structural interrogation on demand and as often as needed. Piezoelectric wafer active sensors (PWAS) are the enabling elements of active SHM systems. PWAS-based SHM can emulate the conventional ultrasonic methods (**pitch-catch, pulse-echo, phased arrays**, etc.) using traveling Lamb waves. (PWAS-based SHM also allows for novel interrogation techniques such as the broad-band standing-waves electromechanical impedance method [1]).

This paper has shown that PWAS can be used to detect crack growth in a thin-wall specimen through a direct ultrasonic imaging technique called *embedded ultrasonics structural radar* (EUSR). Ultrasonic guided waves (Lamb waves) transmitted and received with PWAS transducers have been used in conjunction with the phased-array principle to directly image a thin plate specimen being fatigued in a testing machine. The ultrasonic imaging has been done from a single location on the plate in which a PWAS phased array was installed. The imaging was done

with a scanning beam of ultrasonic guided waves (Lamb waves) traveling in the plate. Thus, crack growth was directly measured from the PWAS EUSR image. The ultrasonic phased-array image was compared with optical photos taken with a digital camera. Thus, a method for direct in-situ imaging of crack growth using permanently attached PWAS transducers has been presented and experimentally verified.

The paper started with a short review of the PWAS transducers principles. Emphasis was placed on PWAS interaction with the guided Lamb waves in the structure, and the PWAS capability to selectively tune into specific Lamb wave modes. Then, it was shown how tuned Lamb wave modes (in particular, the low-dispersion S0 mode) can be used in conjunction with a PWAS phased array to directly image a thin-wall specimen with a steering beam generated in the PWAS array. In our particular application, an ingenious approach was taken to minimize the instrumentation requirements by using only one excitation channel, collecting the data of elemental signals in a round-robin fashion, and then applying the phased array principles in virtual time through signal processing using the EUSR algorithm.

The paper continued with a brief recall of the linear elastic fracture mechanics principles used in the design of the experimental specimen. The aim of this specimen design was to create the conditions under which sizable crack growth can be generated in a plate specimen during a reasonable testing period. Low-cycle fatigue principles, combined with fracture mechanics crack growth theory were used in the specimen design.

After these theoretical preliminaries, the paper presented the experimental setup used during testing. The setup consisted of the testing machine used to apply the cyclic loading and the instrumentation used to collect the PWAS signals. Remarkably, the PWAS signals were collected during actual fatigue testing. To achieve this feat, signal filtering and noise rejection methods had to be applied to extract the weak PWAS signal from the rather large noise created by the cycling testing and adjacent vibrations. The experimental procedure consisted of two steps:

- (a) Validation of the crack growth assumptions, which was done on a plain specimen without PWAS instrumentation; and
- (b) Validation of the PWAS EUSR imaging of crack growth, which was done on a fully instrumented second specimen.

Discussion of the experimental results indicated that the crack growth direct imaging using ultrasonic guided waves and an in-situ PWAS phased array compared very well with the photos of the crack taken with a digital optical camera. Discussion of the results also indicated the limitation of the present method, especially due to the size of the PWAS phased-array aperture, distance from the crack to the array, and crack orientation with respect to the array.

The final section of the paper considered the possible impact of the reported method onto the diagnosis, prognosis, and life prediction of our aging aircraft fleet. Active SHM offers considerable advantages over conventional NDI/NDE performed during strip-down scheduled maintenance. In the near term, SHM technology has the potential to augment current NDI/NDE practices in order to provide supplementary data that will have a densifying effect on the NDI/NDE information pool. This will permit improved prognosis and better remaining life prediction. SHM sensors can be placed in critical locations that would benefit from close monitoring. Thus, unscheduled maintenance will be greatly reduced and even eliminated, contributing a significant reduction in maintenance cost and a great improvement of safety and operational availability. In the long term, SHM may completely replace the current NDI/NDE practice, and eliminate the costly strip-down inspections and the associate removal from operations that impose such a burden on current maintenance practice of current aircraft fleets.

Further research needs to be conducted before PWAS-based SHM could be brought to full fruition. The electromechanical coupling between PWAS and the structural Lamb waves must be fully modeled and understood. This would permit the development of PWAS-based SHM solutions that are optimized for specific structural applications. The durability and survivability of the bond between the PWAS and the structure must be fully characterized. A model must be developed to estimate the bond survivability under various environmental/climatic conditions and to predict its durability in service. This is a complex electrical-mechanical-chemical problem that requires an interdisciplinary approach. In the long-term, the in-situ fabrication of PWAS transducers directly onto the structure is a long-term goal that should be explored. If successful, this research would (a) create a direct atomic bond between the PWAS and the structure; (b) permit the conformal application of PWAS to complex shapes and geometry; and (c) maximize the piezoelectric properties of the PWAS material. This research could be conducted using nanotechnology fabrication techniques. A further direction that needs to be pursued is the integration of the PWAS transducers with the data processing software and wireless communication into small integrated active-sensor units that could be deployed in large numbers onto the monitoring structure. This goal could be pursued through an interdisciplinary effort involving microelectronics and nanotechnologies.

Overall, the results presented in this paper confirm that PWAS transducers technology has a good potential for implementation in active SHM systems. In particular, the direct on-demand ultrasonic imaging of crack growth with

in-situ PWAS transducers and the EUSR method have proven very effective. Further research work should focus on refining the theoretical and experimental results and then testing the method on realistic aerospace structures towards full industrial implementation.

VIII. ACKNOWLEDGMENTS

The financial support of National Science Foundation awards # CMS 0408578 and CMS 0528873, Dr. Shih Chi Liu, program director and Air Force Office of Scientific Research grant # FA9550-04-0085, Capt. Clark Allred, PhD, program manager are gratefully acknowledged.

IX. REFERENCES

- [1] Giurgiutiu, V.; Zagrai, A. N.; Bao, J. (2002) "Piezoelectric Wafer Embedded Active Sensors for Aging Aircraft Structural Health Monitoring", *Structural Health Monitoring – An Int. Journal*, Sage Pub., Vol. 1, No. 1, July 2002, pp. 41-61
- [2] Giurgiutiu, V. (2003) "Lamb Wave Generation with Piezoelectric Wafer Active Sensors for Structural Health Monitoring", SPIE's 10th Annual International Symposium on Smart Structures and Materials and 8th Annual International Symposium on NDE for Health Monitoring and Diagnostics, 2-6 March 2003, San Diego, CA, paper # 5056-17
- [3] Giurgiutiu, V.; Lyshevski, S. E. (2004) *Micro Mechatronics: Modeling, Analysis, and Design with MATLAB*, CRC Press, ISBN 084931593X, 2004
- [4] Raghavan A., Cesnik C. E. S.; "Modeling of piezoelectric-based Lamb-wave generation and sensing for structural health monitoring"; Proceedings of SPIE - Volume 5391 Smart Structures and Materials 2004: Sensors and Smart Structures Technologies for Civil, Mechanical, and Aerospace Systems, Shih-Chi Liu, Editor, July 2004, pp. 419-430
- [5] Bottai, G.; Giurgiutiu, V. (2005) "Simulation of the Lamb Wave Interaction between Piezoelectric Wafer Active Sensors and Host Structure", *SPIE Vol. 5765*, paper # 5765-29 (CD-ROM)
- [6] Giurgiutiu, V.; Bao, J.; Zhao, W. (2003) "Piezoelectric-Wafer Active-Sensor Embedded Ultrasonics in Beams and Plates", *Experimental Mechanics*, Sage Pub., Vol. 43, No. 4, December 2003, pp. 428-449
- [7] Giurgiutiu, V.; Bao, J. (2002) "Embedded Ultrasonic Structural Radar for the Nondestructive Evaluation of Thin-Wall Structures" Proceedings of the 2002 ASME International Mechanical Engineering Congress, November 17-22, 2002, New Orleans, LA, paper # IMECE2002-39017
- [8] Giurgiutiu, V.; Bao, J.; Zagrai, A. N. (2006) "Structural health monitoring system utilizing guided Lamb waves embedded ultrasonic structural radar", U.S. Patent Office #6,996,480 of Feb. 7, 2006
- [9] Yu, L.; Giurgiutiu, V. (2005) "Multi-damage Detection with Embedded Ultrasonic Structural Radar Algorithm using Piezoelectric Wafer Active Sensors through Advanced Signal Processing" *NDE for Health Monitoring and Diagnostics, Health Monitoring and Smart NDE of Structural and Biological Systems Conference*, San Diego, CA, 7-10 March, 2005, paper # 5768-48
- [10] Paris, P. C.; Erdogan, F. (1963) "A critical Analysis of Crack Propagation Laws", *Journal of Basic Engineering*, ASME Transactions, Series D, Vol. 85, No. 4, 1963, pp. 528-534
- [11] Clark, W. G., Jr. (1971) "Fracture Mechanics in Fatigue", *Experimental Mechanics*, September 1971
- [12] Bucci, R. I.; Nordmark, G.; Startke E., A. (1996) *Selecting Aluminum Alloys to Resist Failure by Fracture Mechanisms in Fatigue and Fracture*, ASM Handbook Vol. 19, Lampman, S. R. (Technical Editor), ASM International, Materials Park, OH 44073-0002
- [13] Barsom, J. M. (1972) "Effect of Cyclic Stress Form on Corrosive Fatigue Crack Propagation below K_{ISCC} in High Yield Strength Steel", *Corrosion Fatigue*, 1972, pp. 424-436
- [14] Hartman, A.; Schijve, J. (1970) The Effects of Environment and Load Frequency on the Crack Propagation Law for Macro Fatigue Crack Growth in Aluminum Alloys", *Engineering Fracture Mechanics*, Vol. 1, 1970, pp. 615
- [15] McMillan, J. L.; Pelloux, R. M. N. (1967) "Fatigue Crack Propagation under Program and Random Loads", *ASTM STP-415*, pp. 505
- [16] Shingley, J. E.; Mischke, C. R. (2001) *Mechanical Engineering Design*, (6th Edition), McGraw-Hill, 2001
- [17] Bruhn, E. F. (1973) *Analysis and Design of Flight Vehicle Structures*, Jacobs Publishing, Inc., 1973
- [18] Liu, W.; Giurgiutiu, V. (2005) "Automation of Data Collection for PWAS-based Structural Health Monitoring", *SPIE Vol. 5765*, paper # 5765-129 (CD-ROM)
- [19] Doane, J.; Giurgiutiu, V. (2005) "An Initial Investigation of the Large Strain and Fatigue Loading Behavior of Piezoelectric Wafer Active Sensors", *SPIE Vol 5765*, paper # 5765-130 (CD-ROM)
- [20] Wood, H. A. (1971) "Fracture Control Procedures for Aircraft Structural Integrity", AFFDL Report TR-2-89, WPAFB, Ohio, July 1971
- [21] Rich, T. P.; Cartwright, D. J. (Editors), *Case Studies of Fracture Mechanics*, Report AMMRC MS77-5, US Army Material Development and Readiness Command, Alexandria, VA, 1977
- [22] Cruse, Thomas A. (2004) "Future Directions in NDE and Structural Health Monitoring", *Journal of Nondestructive Evaluation*, Springer Verlag, Vol. 23, No. 3, September 2004, pp. 77-79